Examining deformation localization of irradiated tungsten under uniaxial compression with crystal plasticity

Yuanyuan Wang[1], Xin Sun[2*], Jijun Zhao[1*]

[1] *Key Laboratory of Materials Modification by Laser, Ion and Electron Beams, Dalian University of Technology, Dalian 116024, China*
[2] *Energy Science and Technology Directorate, Oak Ridge National Laboratory, Oak Ridge, TN 37831, USA*

E-mails: sunx1@ornl.gov (X. Sun), zhaojj@dlut.edu.cn (J.J. Zhao).

Abstract

In this work, the deformation behaviors of irradiated tungsten at elevated service temperatures are examined using mechanism-based crystal plasticity finite element framework by considering multiple mechanisms including thermal softening and irradiation hardening. The previously developed mechanism-based crystal plasticity model is first utilized to assess the yield stress of unirradiated and irradiated tungsten upon low temperature irradiation. The engineering stress-strain response under uniaxial compression is then predicted by considering the interplay between deformation-induced dislocation and irradiation-induced defect clusters, and the predicted results agree well with the experimental measurements. Different strain hardening and flow stresses over a wide test temperature range are additionally carried out to provide the reference values. More importantly, the formation and evolution of plastic strain localization zones in the form of shear bands are qualitatively captured, and the maximal principal strain distribution is quantitatively linked to the irradiation damage dose. Finally, the shear band production as a result of plastic instability in tungsten compression specimen is discussed.

Keywords: Irradiation; Damage; Defect clusters; Strain localization; Compression; Finite element

1. Introduction

Tungsten, a prime candidate for plasma-facing material for the first wall of fusion reactors, has excellent physical properties such as high melting temperature and high thermal conductivity. However, its ductile-to-brittle transition temperature (e.g., 550 ℃ for pure tungsten plate [1]) is much higher than other metallic materials (e.g., -81 ℃ for Eurofer97 [2]), reducing its ductility and fracture toughness at elevated service temperature. More seriously, the extreme service environment can also accelerate the degradation of mechanical properties of tungsten due to the generation of irradiation defects [3, 4]. Therefore, more fundamental understandings on the deformation mechanisms of irradiated tungsten and predictive capabilities on the interplays between irradiation-induced defect clusters and deformation-induced dislocations at service temperature must be established before the engineering application of tungsten as plasma-facing material in a fusion reactor.

On the microscopic scale, many prior studies elucidate the different types of irradiation defects for tungsten. While some defect clusters (e.g., small loops) are considered as weak obstacles to dislocation gliding, others act (e.g., voids and bubbles) as strong obstacles to impede the dislocation movement. On the one hand, the moving dislocations generate point defects, the migration of which enhances the formation of short-range orders. On the other hand, the irradiation-induced short-range orders can be annihilated/destructed by the dislocation movement [5]. As a result of this interplay, dislocation channeling is often observed in the deformed metal after irradiation, and it occurs even at low dose since irradiation-induced defect clusters are present in sufficient density [8]. Transmission electron microscopy (TEM) studies confirm that defect clusters are absent in the channels, whilst defect clusters are visible outside the channels [7]. However, the interaction between deformation-induced dislocations and irradiation-generated defect clusters can be quite complex. For example, the high internal stress around the precipitates caused by dislocation accumulation in bcc iron can contribute to the cross-slipped dislocations overcoming irradiation-induced defect clusters [9].

The microscopic interactions of irradiation defects and external loading have also been examined with various modeling and simulation approaches [add some MD references]. For example, MD simulations… [Fei Gao, David Bacon et al….]… Discrete dislocation dynamics (DD) simulation on a single ?? crystal [13] shows the unpinning of irradiation-induced defects are swept away by the dislocation motion, resulting in defect free dislocation channels, and the width of plastic flow localization occurred in dislocation channel can be limited by the interaction among opposing dislocation dipole segments. Even though the microscopic-level simulation results can corroborate the TEM observations in the sense that irradiation-induced defect clusters can be partially removed by interacting with the dislocation [10, 11], leading to defect free channels in the deformed irradiated material [12], they cannot be used to predict the bulk, engineering-level deformation behaviors of irradiated materials.

On the macroscopic engineering scale, many experiments have been carried out to investigate the effects of irradiation-induced microstructure changes on flow stress, hardness and ductility of various polycrystalline bcc, fcc and hcp metals [5-7]. For bcc metals, Byun et al. [6] found that macroscopic plastic instability occurs even though the irradiation dose is one tenth, and deformation localization is typically exhibited in the form of shear bands. It indicates that plastic deformation mainly localizes within these bands as a result of inhomogeneous deformation through the specimen. Consequently, the highly localized flow leads to very low overall ductility. Grain-level material and microstructure heterogeneity has been established as a source for inhomogeneous deformation and strain localization, which can lead to overall sample plastic instability and failure [23]. For irradiated materials, however, the interplays among hardening from irradiation defects, softening from the interaction of mobile dislocations and irradiation defects, and softening due to elevated service temperatures have not been quantitatively established. Dislocation channel that evolves from the deformation dislocations in the localized yielding is one of the possible physics reasons for understanding the strain localization [14]. Strain localization in the form of shear bands is a common deformation mode for nonlinear

materials under compression, and plastic instability may further trigger the shear band formation. In general, the topological feature of shear band is a narrow zone that contains intense shearing strain. This kind of localized strain region is usually an origin of cracking which may eventually lead to final specimen fracture.

Generally speaking, the generation of irradiation-induced defect clusters can greatly increase plastic deformation resistance. The un-irradiated tungsten is known to be resistant to shear banding because of its strong rate sensitivity and high ductile to brittle transition temperature. For ultra-fine grained pristine tungsten, Wei et al. [15] concluded that the kink-pair nucleation on dislocation and its subsequent propagation can reduce the strain rate sensitivity during uniaxial dynamic compression, leading to severe shear localization and the formation of cracks.

As aforementioned analysis, there is no doubt that defect clusters considered as weak/strong obstacles to the dislocation glide require extra force to overcome. Many experimental and theoretical studies focus on irradiation hardening in terms of hardness and macroscopic stress-strain curves, but the underlying deformation mechanisms considering the competition and accommodation of the multiple softening (temperature) and hardening mechanisms (irradiation defects) on macroscopic deformation pattern remain to be revealed. Here, two issues need to be clarified: 1) How the intrinsic features (i.e., size and density) of irradiation-induced defects influence the plastic flow behavior; 2) How the plastic instability triggered by compression loading leads to the shear band formation in irradiated tungsten.

The purpose of present work is to quantitatively investigate the flow stress, strain hardening and deformation modes of pristine and irradiated tungsten with a predictive simulation approach. More specifically, the crystal plasticity finite element model (CPFEM) is used to simulate the irradiation temperature- and dose-dependent stress vs. strain behavior and the associated deformation field under uniaxial compression loading. The previously developed mechanism-based model [16], considering both thermal softening and irradiation hardening, is employed here to assess the yield stress of irradiated tungsten. Accordingly, the microstructure-property relationship of irradiated tungsten is established to predict the plastic deformation behavior. The

CPFEM predicted stress-strain curves are validated by experimental measurements reported in the literature, and the predicted strain localization pattern is also compared with experimental observations.

2. Constitutive model

For crystalline metallic materials, plastic deformation takes place mainly by dislocation glide on crystallographic slip planes. To explore the overall deformation mechanism of (un)-irradiated tungsten, the main crystal plasticity kinematics referred to [16] is adopted. The dislocation motion in the lattice crystal constructs the kinematics part of crystal plasticity theory. The kinematics decomposition of deformation gradient $\boldsymbol{F}$ includes elastic part $\boldsymbol{F}^*$ and plastic part $\boldsymbol{F}^p$ as given by

$$\boldsymbol{F} = \boldsymbol{F}^* \cdot \boldsymbol{F}^p \tag{1}$$

The plastic velocity gradient $\boldsymbol{L}^p$ related to crystallographic slip is written as

$$\boldsymbol{L}^p = \dot{\boldsymbol{F}}^p \boldsymbol{F}^{-1p} = \sum_\alpha \frac{1}{2}(m^\alpha \otimes n^\alpha + n^\alpha \otimes m^\alpha)\dot{\gamma}^\alpha \tag{2}$$

where m^α is the slip direction of slip system α, n^α is the slip plane normal direction in the reference configuration, and $\dot{\gamma}^\alpha$ is the shear strain rate on each slip system α.

The shear strain rate ($\dot{\gamma}$) on each slip system related to the resolved shear stress (τ) and the current value of slip resistance (g) is used to describe the rate-dependent hardening mechanism. It can be expressed by a power law relation as

$$\dot{\gamma}^\alpha = \dot{\gamma}_0 \left| \frac{\tau^\alpha}{g^\alpha} \right|^{1/m} sign\left(\frac{\tau^\alpha}{g^\alpha} \right) \tag{3}$$

where $\dot{\gamma}_0$ is the reference shear strain rate assumed as 0.001, and m is a rate sensitivity coefficient and is used as 0.5. As for the dislocation loop-containing tungsten, the nature of crystal strain hardening is considered as a result of the slip-slip

interactions which can be represented by an interaction matrix $h_{\alpha\beta}$. The strain hardening rate ($\dot{g}$) is

$$\dot{g}^{\alpha} = \sum_{\beta} q^{\alpha\beta} h_0 sech^2 \left| \frac{h_0 \gamma}{\tau_s - \tau_0} \right| \dot{\gamma}^{\beta} \tag{4}$$

where h_0 is the initial hardening modulus at the initial yield point, γ is the cumulative shear strain on all slip systems, τ_0 is the initial shear stress, and τ_s is the saturation shear stress.

It is important to highlight the microstructure evolution of tungsten during irradiation at low temperature, which determines the macroscopic mechanical responses. On a basis of the experimental observation, dislocation loop is the main irradiation-induced defect in tungsten when temperature is less than 773 K and damage dose is in a range of 0.03-1.62 dpa [17]. This feature induces resistance to slip movement, requiring a higher critical resolved shear stress (τ_0) for dislocation to propagate across the obstacles. Moreover, metallic materials deformed under elevated temperature can show the thermal softening phenomenon since the dislocation kinetics and interactions are enhanced, and tungsten is no exception. These two factors can significantly influence the competition between dislocation generation and dislocation annihilation.

Wang et al. [16] developed a mechanism-based strength model to describe the irradiation and temperature effects on the yield stress of irradiated tungsten (σ^{y}_{irr}), expressed as the linear superposition of the yield strength of un-irradiated material at room temperature ($\sigma^{y}_{unirr,room}$), the yield stress variation caused by irradiation ($\Delta\sigma^{y}_{irr}$) and the effect of temperature on the yield stress ($\Delta\sigma^{y}_{thermal}$). The Johnson-Cook model [18] and the Friedel-Kroupa-Hirsch (FKH) model [19, 20] are chosen to described the thermal softening and irradiation hardening, respectively. The final expression is given as

$$\sigma_{irr}^{y} = \sigma_{unirr,room}^{y} + \Delta\sigma_{irr}^{y} - \Delta\sigma_{thermal}^{y} = (1 - T^{*k})\sigma_{unirr,room}^{y} + \frac{1}{8} f\mu b D(N)^{2/3} \quad (5)$$

where T^* is the homologous temperature, k is the thermal softening exponent, f is the Taylor factor, μ is the shear modulus, b is the Burgers vector of the dislocation, N is the number of dislocation loop, and D is the size of dislocation loop. The homologous temperature can be expressed as $T^* = (T - T_{ref})/(T_m - T_{ref})$, where T_{ref} is the reference temperature and is used as 298 K, T_m is the melting point and is equal to 3673 K in this case study. In this study, the values of N and D are calculated from the set of defect kinematics equations and relevant thermodynamics material parameters (such as migration energy) reported in Ref. [16] in quantifying the formation and evolution of dislocation loops.

3. Finite element implementation

The aforementioned crystal plasticity constitutive equations are incorporated into finite element software ABAQUS via UMAT subroutine to model the deformation behavior. The representative volume element (RVE), i.e., the simulation domain, is composed of 8×8×8 randomly oriented grains with each grain dimension of 26 μm×26 μm×30 μm as shown in Fig. 1(a). 512 initial orientations of grains are randomly assigned, see Fig. 1(b). Each grain is sub-divided into 3×3×3 cubic elements with element type C3D8. To simulate the uniaxial compression loading, the bottom surface (z=0 μm) is constrained from displacement in the z-direction, and a uniform displacement-controlled boundary condition is applied to the top surface (z=208 μm) along the z-axis with a strain rate of 1.0×10^{-3} s^{-1} (see Fig. 1(c)). The slip systems in bcc pristine tungsten can take place on {110}<111>, {112}<111> and {123}<111>, depending on internal (i.e., purity) and external (i.e., temperature) properties. At low-temperature irradiation, the generated dislocation loops with 1/2<111> slip direction on {110} and {112} slip planes are commonly observed in tungsten. Based on above analysis, 24 slip systems, including 12{110}<111> and 12{112}<111>, are utilized in the model to capture the deformation behavior of (un)-irradiated tungsten.

With the increase of uniaxial deformation displacement, the accumulated resolved shear stress on each slip system can reach to a threshold value, activating the slip motion. For a single-crystal case, this critical resolved shear stress can be related to the yield stress of an ordinary stress-strain curve. The Schmid's law gives the relationship between yield stress and critical resolved shear stress (the value of critical resolved shear stress is equal to that of initial shear stress (τ_0)) in the following expression $\tau_0 = \cos\varphi \cos\lambda \sigma^y$ (where φ is the angle between the slip plane normal and the loading axis, and λ is the angle between slip direction and loading axis). Here, the Schmid factor $\cos\varphi\cos\lambda$ is chosen as 0.5 according to the studies of a single-crystal tungsten [21]. Once the yield stress calculated from equation (5) is known, the initial shear stress (τ_0) can be readily estimated. Table 1 lists the calculated yield stress and the corresponding initial shear stress. Other hardening parameters in Eq.(4) are estimated with τ_0 by assuming the ratio of (τ_s/τ_0) as 1.31 and (h_0/τ_0) as 1.42.

4. Results and discussions

4.1 Representativeness of RVE

In order to verify the grain orientation randomness of the RVE, the displacement-based loading condition is applied in all x-, y- and z-axial directions to the RVE to predict the plastic flow stress and strain hardening behaviors of un-irradiated tungsten under uniaxial compressive loading at 748 K. The results are comparatively plotted in Fig. 2. No noticeable difference is observed among the stress-strain responses of the three loading directions, confirming the random grain orientation of the RVE and the FEM implementation of the crystal plasticity framework.

4.2 Irradiation dose and temperature effects on defect size, density and flow stress

Since the experimentally measured mechanical data is obtained following a specific irradiation and test sequence, the simulation steps performed here follows the same steps to understand the engineering stress and strain responses of irradiated tungsten under the uniaxial compression using the crystal plasticity finite element framework described above [16]. First, the predicted diameter and density of irradiation-induced dislocation loops are shown in Fig. 3(a). Under both irradiation temperatures, the diameters of the dislocation loops increase with the damage dosage, but higher temperature leads to larger loops and higher growth rate of the loop size. Conversely, under the same damage dosage, the density of the dislocation loops decreases with increasing irradiation temperature, and there seems to exist a unique transition dosage level for temperature above which the growth of loop density slows down dramatically.

Next, these simulated defect data is used in Eq. (5) to calculate the yield stress for the two irradiated samples irradiated at 3 dpa under 318 K and at 22.5 dpa under 495 K. The contributions from thermal softening and irradiation hardening are both taken into account compared to the un-irradiated case. The compressive experimental data from 99.95% purity tungsten with hot press pre-treatment [22] is utilized to examine our predicted yield stress plotted in Fig. 3(b). At a deformation temperature of 748 K, the corresponding calculated yield stress of un-irradiated tungsten is approximate 467 MPa. Once the sample is subjected to irradiation conditions of 3 dpa under 318 K and 22.5 dpa under 495 K, the corresponding yield stresses reach to 897 MPa and 1276 MPa, respectively. Since much larger dislocation loops form and grow in the sample with higher damage dose, higher external force is needed for the deformation-induced dislocations to overcome these initial obstacles, leading to higher yield stress (see Eq. (5)). These results match well with the experimentally measured data 895 MPa and 1337 MPa, reported in the literature [22].

In addition to the yield stress, Fig. 3(b) also predicts different flow stress (continuous lines) and hardening behaviors for the two irradiated samples under the same uniaxial compressive loading at 748 K. Compared with experimental data

(discrete squares), both yield stress and overall hardening behaviors are well captured for the three samples under different irradiation conditions. Comparing the curves in Fig. 3(b), the intrinsic features of dislocation loop play a dominant role in determining the irradiation hardening. Among the three sample, the unirradiated tungsten has the highest hardening slope. For irradiated tungsten, because the irradiation-induced defects and short-range orders can be annihilated/destructed by the dislocation movements, the resulted hardening slopes are lower than the unirradiated case.

4.3 Irradiation dose effects on maximum principal strain

The significant changes of mechanical properties of irradiated metals, especially yield strength increase and hardening slope decrease, are often accompanied by early plastic flow localization and reduced ductility [13]. In order to assess the effect of irradiation on the evolution of plastic flow, the typical contour maps of dose-dependent maximum strain for 0 dpa, 3 dap and 22.5 dpa dose levels are plotted in Fig. 4(a)−(c), respectively. Here, the contour map of maximum principal strain at 20% compression deformation across 64 grains meshed by 3×3 elements on the *x*-*z* plane at *y*=208 μm is plotted to illustrate the inhomogeneous deformation mode. An obvious shear band pattern is captured in both irradiated and un-irradiated cases, which indicates the main deformation mode of tungsten under compression is in the form of plastic flow localization (or plastic instability). The regions surrounding the shear bands are usually much less strained, typically by one order of magnitude. The macroscopic shear bands can penetrate through two or more grains, resulting in severe intra- and inter-granular distortion. Although tungsten is a bcc metal with high intrinsic stacking fault energy, the resistance of the grain boundary to the dislocation motion may be weak. But boundary sliding is not considered in this study, right? Grain boundaries are treated as coherent without the possibility of cracking, right? We need to point out…

The distribution of maximum principal strain in Fig. 4(a)-(c) has another common feature, i.e., the high strain level appears both on the grain boundary and in the grain interior due to the dislocation pile-up at these locations. In general, high

strain field is accompanied by high stress concentration as it is induced by dislocation pile-ups [24]. Grain boundary acts as an obstacle to the movement of dislocation during plastic deformation, causing the formation of numerous dislocation arrays near the grain boundary. The dislocation pile-ups can provide a larger shear strain on equally dislocations and active slip planes. This leads to the complex and variable local stress and strain field near and off grain boundary when strained. Different from grain boundary, the atom arrangement within the grain interior is highly ordered, and the plastic deformation is completely accommodated by dislocation slip on the relevant plane. Consequently, the stress and strain fields of the grain interior is usually homogeneous. However, for irradiated metals, dislocation pile-up may appear in grain interior due to local perturbations by irradiation-induced clusters, generating local stress and strain gradients. While MD or DD-level simulations can resolve the dislocation pile-up induced gradients and their interactions with the complex stress field by the incoherent phase boundary [25], the crystal plasticity framework implemented in this study does not explicitly capture the defect/dislocation interactions within the grain. Rather, the stress state of each uniquely orientated grain is calculated by subjecting the entire RVE to the overall external loading while satisfying the deformation compatibility and free surface conditions [26].

Although the defect is assumed to be uniformly distributed at the grain level, noticeable differences can be decerned at the macroscopic scale for samples with different irradiation levels. Comparing Figs. 4(a), (b) and (c), a slightly higher degree of plastic deformation inhomogeneity can be observed for higher doses. This irradiated microstructure-dependent localized deformation is consistent with experimental observations [27]. Other numerical simulations (e.g., discrete dislocation dynamics) have also confirmed that the homogeneity of plastic slip activity is reduced with increased irradiation dose [28, 29], which can be mainly attributed to the increased grain-level heterogeneities due to the increased resistance to plastic slip in each grain with different features (i.e., density and size) of irradiation defect clusters. With increasing dose, more point defects are generated in the microstructure, and higher slip resistance required for dislocation motion for that grain.

Fig. 4(d) attempts at quantifying the degree of strain localizations under different irradiation dosage with the statistical distribution of local maximum principal strains for the three cases above. It is found that the local strain distribution follows the lognormal distribution irrespective of pre-existing irradiation-induced defect clusters. This lognormal distribution characteristic has been discovered by Tang et al. [30] on conventional steels without irradiation, and a standard lognormal expression can be used to quantitatively assess the strain value and the relevant frequency. From our compressive results of (un)-irradiated tungsten, two obvious features in Fig. 4(d) are summarized by comparing with the strain distribution of pristine tungsten as the baseline: First, the peak of the strain distribution curve shifts to a higher strain value as irradiation dose increases, i.e., ε_{mp}=0.152 (0 dpa), ε_{mp}=0.160 (3.0 dpa) and ε_{mp}=0.166 (22.5 dpa); Second, the peak value of lognormal curve (marked as frequency (F)) decreases with increasing irradiation dosage, i.e., F=29.08% (0 dpa), F=28.23% (3.0 dpa) and F=26.78% (22.5 dpa).

In general, the variation and evolution of strain distribution curves depend on the loop-dislocation interaction in irradiated microstructure. For bcc metals, the loop behaves as Orowan obstacle, and it cannot be absorbed by dislocation at low temperature. At high temperature, however, the bypassing mechanism is replaced by the complete loop absorption [31]. For strong obstacle, the critical stress (τ_c) is related to loop size and defect density as (is there a reference?):

$$\tau_c = \frac{Gb}{2\pi L}\left[\ln\left(D^{-1}+L^{-1}\right)^{-1}+B\right] \tag{6}$$

where G is the effective shear modulus, b is the Burgers vector, B is a constant that depends on the nature of the obstacle, D is the obstacle size, L is the distance between neighboring obstacles. Compared with loops in small size and high density (e.g., at 318 K with a dose of 3 dpa), the large loop size with low loop density (e.g., at 485 K with a dose of 22.5 dpa) needs more applied stress to overcome. Accordingly, the range of local maximum principal strain move toward to a higher strain level.

4.4 Irradiation dose effects on deformation field evolution

To better illustrate the plastic flow evolution in irradiated tungsten during compression, tungsten irradiated at 318 K with 3.0 dpa and subsequently compressed at 748 K is taken as an example. The contour maps of maximum principal strain at 5%, 10%, 15% and 20% overall compressive strains are shown in Figs. 5(a), (b), (c) and (d), respectively. Following the displacement-controlled loading, macroscopic inhomogeneous deformation within the represent volume element appears clearly at high strain level, accompanied by the formation of visible shear bands. At strain level of 10% (Fig. 5(b)), several highly strained (green) regions appear sporadically distributed in the contour map. At ε=20%, the morphology of macroscopic shear bands in Fig. 5(d) is clearly visible, which agrees well with the optical micrograph image from the corresponding experiment (Fig. 5(e)) [22]. It is worthy pointing out that plastic flow is more likely to localize in the bands, in which high strains are concentrated.

As reported by [33], shear band is a narrow zone of strain localized by inhomogeneous deformation field and accompanied by global softening and load drop, leading to final sample failure. The shear band inclination is affected by the predefined glide systems corresponding to the predefined grain orientation, and the model aspect ratio is also a key factor. In the current study, the inclination of the shear band with respect to the plane orthogonal to the loading direction is in the range of 36-45°. In addition, a series of parallel strain localization bands are predicted at ε=20%, similar to the propagation of band-like configuration over the surface of specimen in Fig. 5(e). It indicates that a localized event of a single band between plastically deformed and undeformed region that moves with the constant cross head velocity. A macroscopic crack is also observed initiating from a shear band in Fig. 5(e), which indicates that plastic flow localization within the shear band is more likely to lead to crack formation at the surface of a weaker grain. On the other hand, the crack may form at many locations prior to the plastic instability, since the ductile-to-brittle temperature of irradiated tungsten is very high.

The contour maps in Fig. 5(a)-(d) also suggest that the high degree of strain localization at the sample free surface can accelerate the formation of macroscopic shear bands. Coincidentally, inhomogeneous nucleation of dislocation from free surface in pristine tungsten nanowires during compression loading is experimentally observed by *in-situ* TEM nanomechanical testing and theoretically calculated by ?? dynamics simulation [32]. In general, grain boundaries as well as free surfaces can act as hard barriers for dislocation glide during plastic deformation and therefore become a hot spot for strain localization.

The evolutions of von Mises stress and maximum principal strain at different overall strain levels are shown in Fig. 6(a) and (b), respectively, on the deformed sample geometry for the three samples under irradiation damage dosages of 0 dpa, 3 dpa, 22.5 dpa. With increasing overall compressive strain, the overall stress distribution becomes more inhomogeneous for all three samples, but the maximum stress level ranges from 2151 MPa for the unirradiated sample to 4347 MPa for the 22.5 dpa sample at 20% of overall compressive strain level. In addition, the stress concentration occurs not only at the grain boundary but also in the grain interior. The RVEs' free surfaces (left and right) change from initial smooth to wavy configurations for all the three samples with increasing strain due to grain rotations to the preferred orientation during deformation, although the magnitude of the surface waviness slightly increases with irradiation dosage. Different from the stress contours, Fig. 6(b) shows that maximum principal strain is localized in a continuous band for all the three cases starting from overall compressive strain level of 10%, with much higher strain level developed within such deformation bands than elsewhere in the RVE. Although the damage dosage ranges from 0-22.5 dpa, the characteristics of the strain contours are very similar for the three samples, with the strain levels slightly enhanced at higher dosages.

4.5 Predicted temperature effects on irradiated tungsten under compression

In this section, we use the established crystal plasticity finite element framework to predict the effects of different test temperatures (i.e., 298 K, 548 K, 748 K and 948

K) on the compressive stress vs. strain behaviors of the sample irradiated at 495 K with a damage dosage of 3 dpa. Fig. 7(a) illustrates the calculated contributions to σ_{irr}^{y} according to the established mechanism-based model (Eq. (5)) for all four test temperatures. Because the same irradiated sample is used, the contributions from $\sigma_{unirr,room}^{y}$ and $\Delta\sigma_{irr}^{y}$ on σ_{irr}^{y} are the same, and the predicted σ_{irr}^{y} decreases with increasing test temperature due to the thermal softening term $\Delta\sigma_{thermal}^{y}$.

Fig. 7(b) shows the predicted stress-strain responses under compression for the four test temperatures. The simulation results show that both yield stress and hardening slope decrease with increasing test temperature, quantitatively illustrating that thermal softening plays a significant role in strain hardening of irradiated tungsten.

4.6 Predicted temperature effects on irradiated tungsten under tensile loading

5. Conclusion

In this study, we examine the inhomogeneous deformation behaviors of irradiated tungsten under uniaxial compression at low deformation temperature. The previously developed mechanism-based crystal plasticity model implemented with finite element framework is used to resolve the overall deformation behavior of the RVE and the responses of each grain. The temperature- and dose-dependent irradiation-induced loop size and density are evaluated and used in the determination of irradiation hardening. The main findings are summarized as follows:

1) The deformation behavior and mechanical property of the RVE depend on the irradiation-induced microstructures, and the predicted macroscopic stress-strain relationships for (un)-irradiated tungsten are in reasonable agreement with experimental results.
2) Higher irradiation dosage leads to larger defect clusters, hence higher levels of inhomogeneity and resistance to dislocation glide within the

grain, shifting the overall RVE maximum principal strain distribution curve to a higher level.

3) The predicted strain localization bands and wavy feature of sample free surfaces correspond well with experimental observations for compressed tungsten, qualitatively explaining the sources of the shear band formation which can eventually lead to cracking.

It should be mentioned that mesh-size dependent strain prediction is a natural outcome of the grid-based finite element method in resolving the strain magnitude within the localized deformation bands. Sun et al. [23] presented a systematic study and concluded that the finer uniform mesh can predict much earlier onset of plastic strain localization and a steeper post-critical slope compared to the uniform coarse mesh for multiple steel sample under uniaxial tensile loading. The purpose of this work is to understand the inhomogeneous plastic deformation mechanisms of irradiated tungsten under uniaxial compression loading, and the analysis presented is applicable to defect clusters in the form of dislocation loops. As shown in the literature, other types of defects such as voids, bubbles and precipitates can also be generated in irradiated tungsten under a certain temperature range and damage dosages. Future studies should be extended on considering the effect of other clusters-dislocation interaction on the fundamental deformation behavior of metallic materials.

Data availability

The raw/processed data required to reproduce these findings cannot be shared at this time as the data also forms part of an ongoing study.

Acknowledgement

This work was supported by the National MCF Energy R&D Program (2018YFE0308100, 2018YFE0308105), the National Natural Science Foundation of China (11905025) and the Fundamental Research Funds for the Central Universities (DUT19RC(3)068, DUT20ZD207). Oak Ridge National Laboratory is operated by UT-Battelle, LLC, for the U.S. Department of Energy under contract DE-AC05-00OR22725. We acknowledge the computational support from the Supercomputing Center of Dalian University of Technology.

References

[1] S. Nogami, A. Hasegawa, M. Fukuda, M. Rieth, J. Reiser, G. Pintsuk, Journal of Nuclear Materials, 543 (2021) 152506.
[2] E. Gaganidze, H.C. Schneider, B. Dafferner, J. Aktaa, Journal of Nuclear Materials, 367-370 (2007) 81-85.
[3] D. Terentyev, M. Vilémová, C. Yin, J. Veverka, A. Dubinko, J. Matějíček, International Journal of Refractory Metals and Hard Materials, 89 (2020) 105207.
[4] L.M. Garrison, Y. Katoh, N.A.P.K. Kumar, Journal of Nuclear Materials, 518 (2019) 208-225.
[5] V.A. Shabashov, K.A. Kozlov, A.L. Nikolaev, A.E. Zamatovskii, V.V. Sagaradze, E.G. Novikov, K.A. Lyashkov, Philosophical Magazine, 100 (2020) 1-17.
[6] T.S. Byun, K. Farrell, Acta Materialia, 52 (2004) 1597-1608.
[7] K. Wang, Y. Dai, P. Spätig, Journal of Nuclear Materials, 468 (2016) 246-254.
[8] N. Hashimoto, T.S. Byun, K. Farrell, S.J. Zinkle, Journal of Nuclear Materials, 329-333 (2004) 947-952.
[9] C. Robertson, K. Gururaj, Journal of Nuclear Materials, 415 (2011) 167-178.
[10] J.S. Robach, I.M. Robertson, H.J. Lee, B.D. Wirth, Acta Materialia, 54 (2006) 1679-1690.
[11] D.J. Bacon, F. Gao, Y.N. Osetsky, Journal of Nuclear Materials, 276 (2000) 1-12.
[12] D. Kiener, P. Hosemann, S.A. Maloy, A.M. Minor, Nature materials, 10 (2011) 608-613.
[13] T. Diaz de la Rubia, H.M. Zbib, T.A. Khraishi, B.D. Wirth, M. Victoria, M.J. Caturla, Nature, 406 (2000) 871.
[14] M.D. McMurtrey, G.S. Was, B. Cui, I. Robertson, L. Smith, D. Farkas, International Journal of Plasticity, 56 (2014) 219-231.
[15] Q. Wei, T. Jiao, K.T. Ramesh, E. Ma, L.J. Kecskes, L. Magness, R. Dowding, V.U. Kazykhanov, R.Z. Valiev, Acta Materialia, 54 (2006) 77-87.
[16] Y. Wang, X. Sun, J. Zhao, Materials Science and Engineering: A, 774 (2020) 138941.

[17] Q. Xu, N. Yoshida, T. Yoshiie, Journal of Nuclear Materials, 258 (1998) 1730-1734.
[18] G.R. Johnson, W.H. Cook, Engineering Fracture Mechanics, 21 (1985) 31-48.
[19] J. Friedel, The London, Edinburgh, and Dublin Philosophical Magazine and Journal of Science, 46 (1955) 1169-1186.
[20] F. Kroupa, P. Hirsch, Discussions of the faraday Society, 38 (1964) 49-55.
[21] H. Lim, C.C. Battaile, J.D. Carroll, B.L. Boyce, C.R. Weinberger, Journal of the Mechanics and Physics of Solids, 74 (2015) 80-96.
[22] S.A. Maloy, M.R. James, W. Sommer, G.J. Willcutt, M. Lopez, T.J. Romero, M.B. Toloczko, Journal of Nuclear Materials, 343 (2005) 219-226.
[23] X. Sun, K.S. Choi, W.N. Liu, M.A. Khaleel, International Journal of Plasticity, 25 (2009) 1888-1909.
[24] K. Fukuya, H. Nishioka, K. Fujii, T. Miura, T. Torimaru, Journal of Nuclear Materials, 417 (2011) 958-962.
[25] R. Li, Y.-D. Wang, W. Liu, C. Geng, Q. Xie, D.E. Brown, K. An, Acta Materialia, 165 (2019) 336-345.
[26] V.A. Romanova, R.R. Balokhonov, S. Schmauder, Materials Science and Engineering: A, 564 (2013) 255-263.
[27] Z. Jiao, G.S. Was, Journal of Nuclear Materials, 407 (2010) 34-43.
[28] J. Hure, S. El Shawish, L. Cizelj, B. Tanguy, Journal of Nuclear Materials, 476 (2016) 231-242.
[29] Y. Cui, G. Po, N.M. Ghoniem, International Journal of Plasticity, 104 (2018) 54-67.
[30] A. Tang, H. Liu, G. Liu, Y. Zhong, L. Wang, Q. Lu, J. Wang, Y. Shen, Physical Review Letters, 124 (2020) 155501.
[31] D. Terentyev, Y.N. Osetsky, D.J. Bacon, Scripta Materialia, 62 (2010) 697-700.
[32] J. Wang, Y. Wang, W. Cai, J. Li, Z. Zhang, S.X. Mao, Scientific Reports, 8 (2018) 4574.
[33] J. Pan, Q. Chen, L. Liu, Y. Li, Acta Materialia, 59 (2011) 5146-5158.

Table 1 Material parameters used in the compression simulation performed at 748 K.

Irradiation condition	Mechanism-based strength model				Constitutive model		
	$\sigma^{y}_{unirr,room}$ (MPa)	$\Delta\sigma^{y}_{thermal}$ (MPa)	$\Delta\sigma^{y}_{irr}$ (MPa)	σ^{y}_{irr} (MPa)	τ_0 (MPa)	h_0/τ_0	τ_s/τ_0
0 dpa	1317	850	0	467	225	1.33	1.30
318 K, 3 dpa	1317	850	430	897	447	1.33	1.31
495 K, 22.5 dpa	1317	850	809	1276	668	1.32	1.31

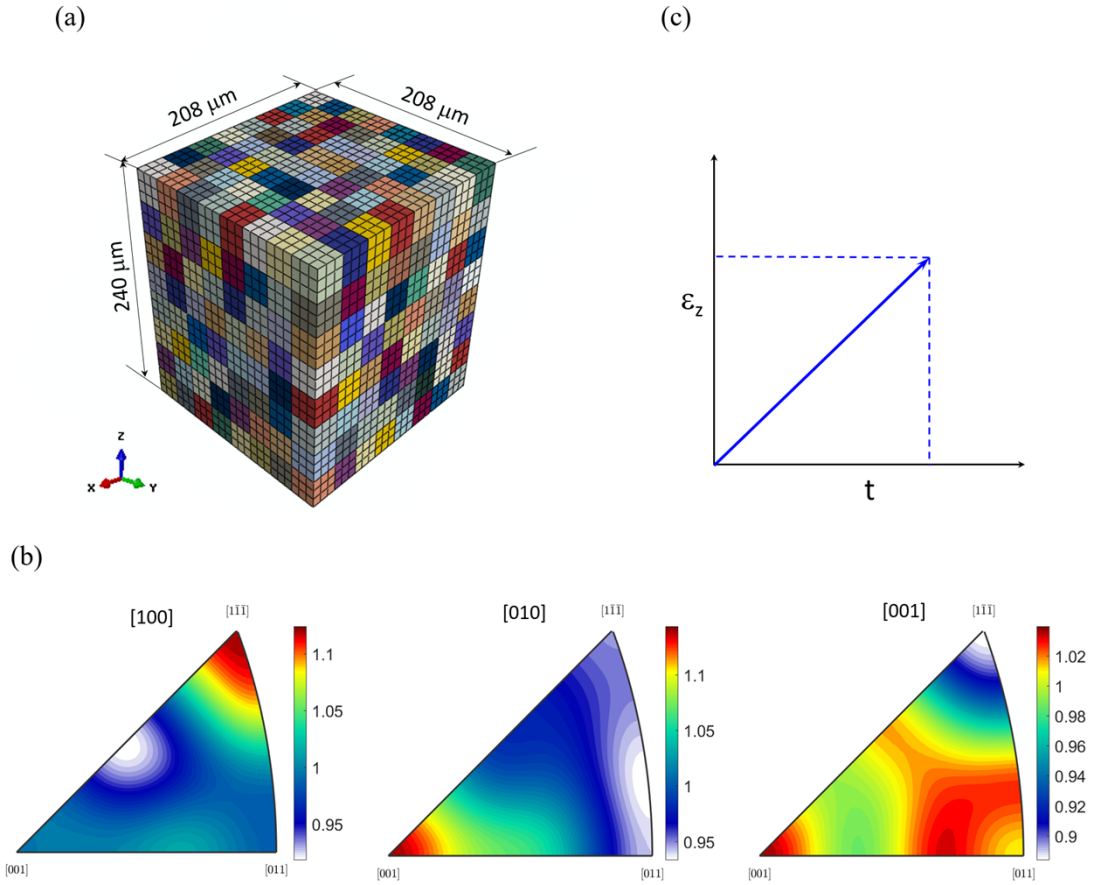

Figure 1. (color online) (a) Polycrystal model with 512 grains with orientation randomness. The size is 26×26×30 μm^3 for each grain, and the mesh is divided into 3×3×3 cubic elements. (b) Inverse pole figures showing the texture on a randomly selected orientations. (c) The uniaxial uniform loading is applied to z-direction.

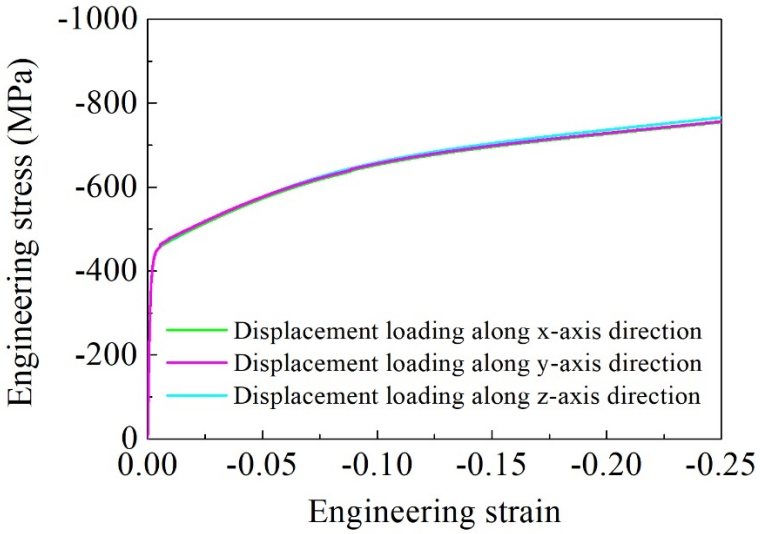

Figure 2. (color online) Predicted stress-strain curves under three different loading directions for the RVE for unirradiated tungsten under 748 K compression.

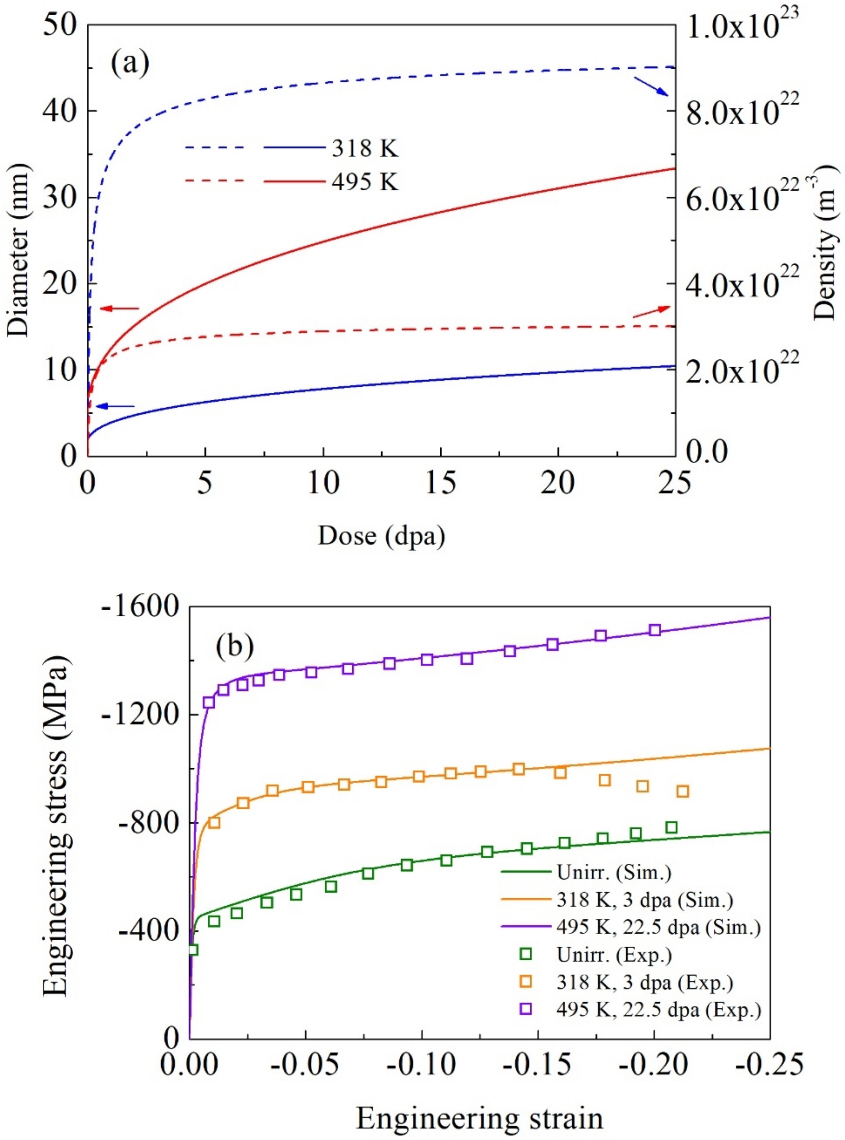

Figure 3. (color online) (a) Dose dependence of diameter and density of dislocation loops at the irradiation temperatures of 318 K and 495 K [16]; (b) Predicted engineering stress and strain responses of irradiated polycrystalline tungsten under compression at 748 K, compared with experimentally measured data [22].

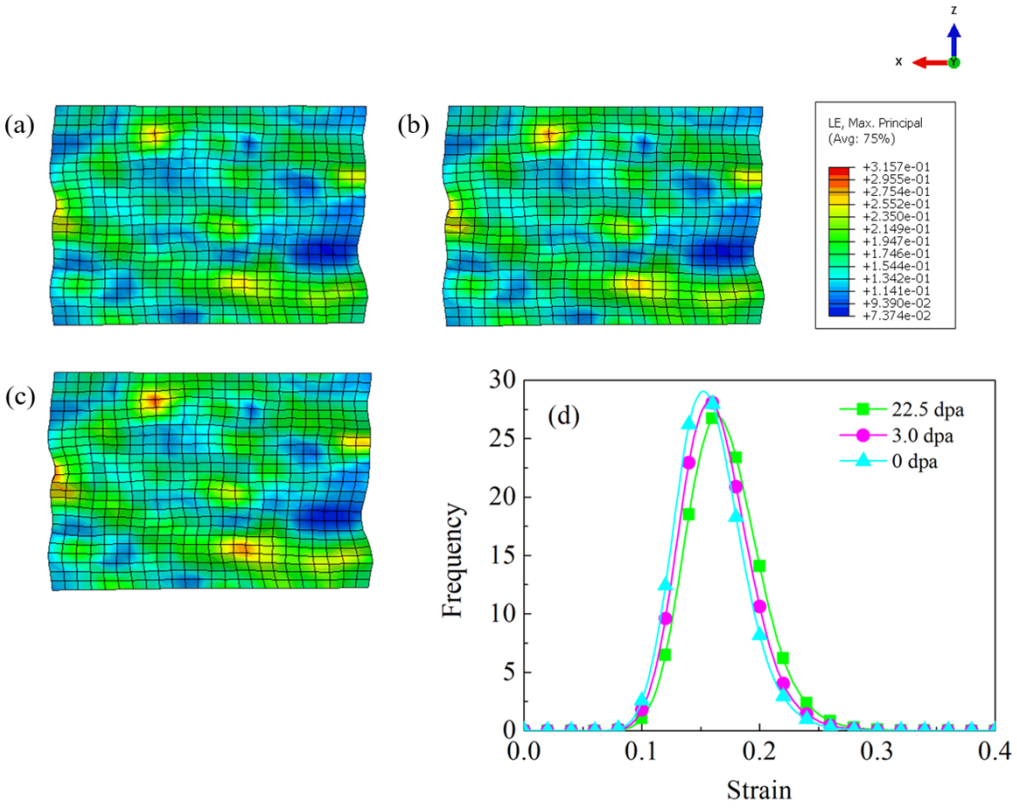

Figure 4. (color online) Contour plot of maximum principal strain at 748 K as a function of irradiation damage level: (a) 0 dpa, (b) 3 dpa and (c) 22.5 dpa. The snapshots are taken in the *x*-*z* plane at y = 208 μm after 20% compression along *z*-axis. (d) Distribution of the maximum principal strain exhibited by the above deformed model.

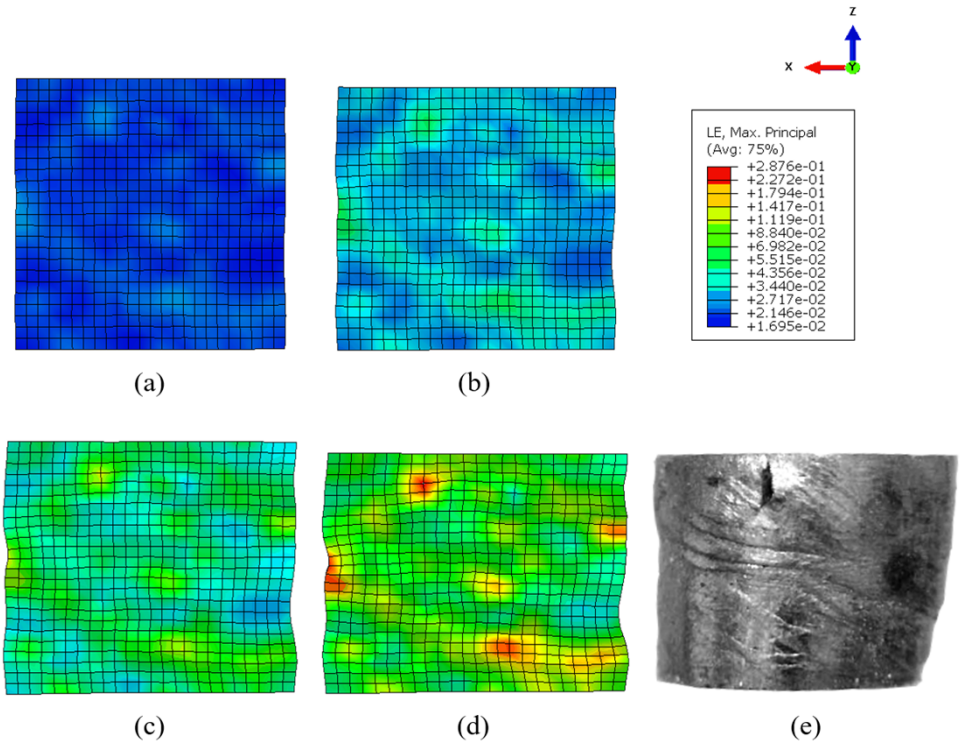

Figure 5. (color online) Contour plot of maximum principal strain in the *x*-*z* plane at *y*=208 μm after (a) ε=5%, (b) ε=10%, (c) ε=15%, (d) ε=20% under compression loading along *z*-axis and (e) optical micrograph of tungsten compression specimens 20% deformation at 748 K and 3.0 dpa [22].

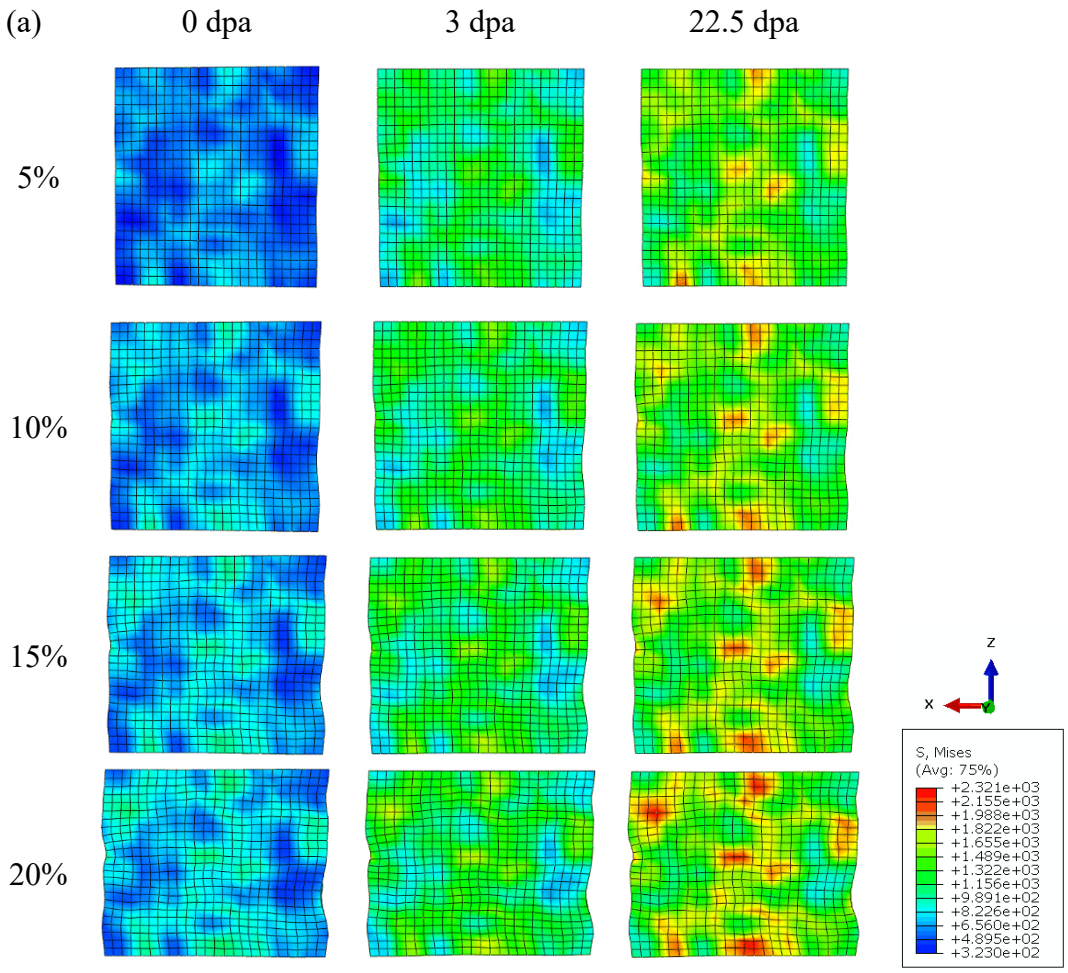

(continue to the next page)

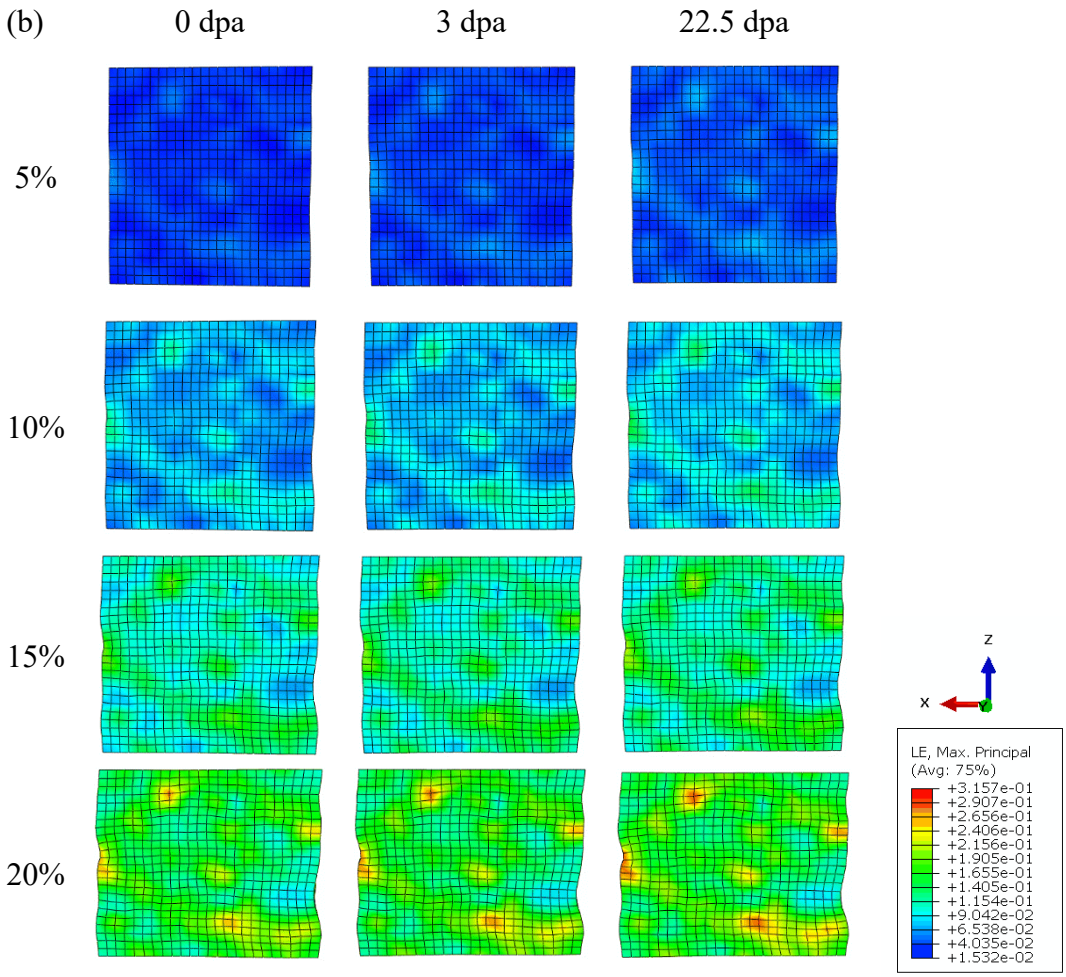

Figure 6. (color online) Comparison of (a) von Mises stress and (b) maximum principal strain distributed in the deformed shape at y=208 μm. The compression simulations are performed at 748 K after different irradiation damage levels.

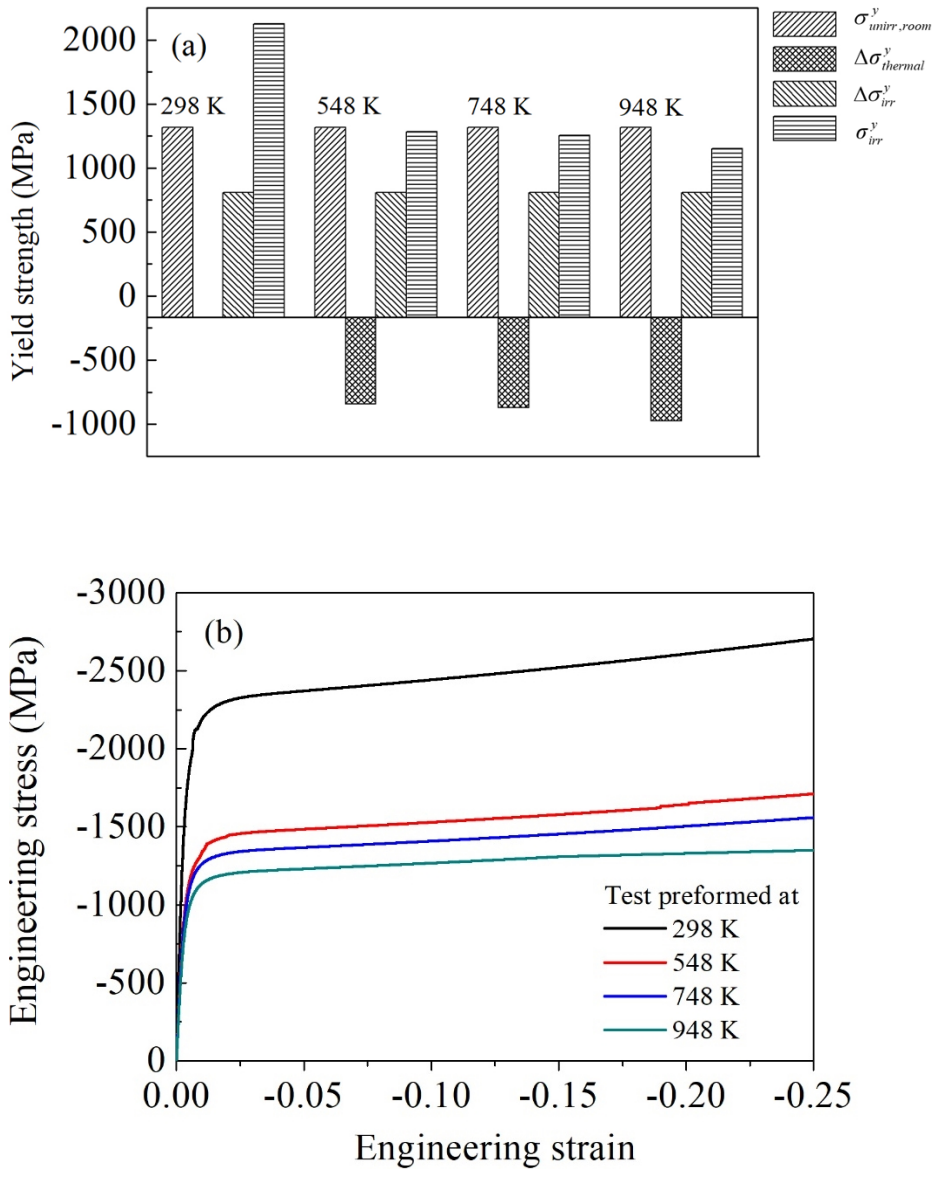

Figure 7. (color online) (a) Predicted contribution to yield strength changes from thermal softening and irradiation hardening and (b) the corresponding simulated stress-strain responses at different compression temperatures for the sample irradiated at 495 K with a damage level of 3 dpa.